Journal of Computational Physics 227 (2008) 9727–9741

Contents lists available at ScienceDirect

Journal of Computational Physics

journal homepage: www.elsevier.com/locate/jcp

Numerical simulation of dealloying by surface dissolution via the evolving surface finite element method

C. Eilks [a], C.M. Elliott [b,*]

[a] Abteilung für Angewandte Mathematik, University of Freiburg, Hermann-Herder-Straße 10, D-79104 Freiburg i. Br., Germany
[b] Mathematics Institute, University of Warwick, Zeeman Building, Coventry CV4 7AL, United Kingdom

ARTICLE INFO

Article history:
Received 28 January 2008
Received in revised form 23 July 2008
Accepted 29 July 2008
Available online 14 August 2008

MSC:
65M60
65Z05

PACS:
02.70.Dh
64.75.Jk
64.75.Op
81.16.Rf

Keywords:
Surface dissolution
Nanoporosity
Spinodal decomposition
Evolving surface finite element method
Cahn-Hillliard

ABSTRACT

In this article we formulate a numerical method for the simulation of dealloying of a binary alloy by the selective removal of one component via electrochemical dissolution such that there is phase separation of the other component at the solid/electrolyte interface. The evolution of the interface is modelled by a forced mean curvature flow strongly coupled to the solution of a Cahn-Hilliard equation modelling surface phase separation. The method is based on a triangulated hypersurface whose evolution is calculated as well as the solution of the Cahn-Hilliard equation by the evolving surface finite element method (ESFEM). The numerical experiments simulate complex morphology and concentration patterns providing evidence that the mathematical model may describe the formation of nanoporosity.

1. Introduction

We study surface pattern formation in the dealloying of a binary alloy by the selective removal of one component via electrochemical dissolution in an electrolyte such that there is surface phase separation of the other component. The model was proposed in order to study the evolution of nanoporosity in the selective electrolytic dissolution of an alloy, [15,16]. A prototypical example is that of the etching of silver in an Ag–Au alloy whose surface is immersed in an electrolyte. The dissolution of silver atoms occurs at the alloy/electrolyte interface while the surface gold atoms diffuse on the surface, agglomerate in clusters and expose the next layer of silver atoms for dissolution. The result is the growth of porosity into the bulk. The model developed in [15] comprises an evolution equation for the time dependent two dimensional hypersurface $\Gamma = \Gamma(t)$

$$V_v = -J_{\text{diss}}, \tag{1.1}$$

* Corresponding author.
E-mail addresses: carsten@mathematik.uni-freiburg.de (C. Eilks), c.m.elliott@warwick.ac.uk (C.M. Elliott).

0021-9991/$ - see front matter © 2008 Published by Elsevier Inc.
doi:10.1016/j.jcp.2008.07.023

and a surface diffusion equation

$$\dot{c} = V_v c_b - \nabla_\Gamma \cdot J_{diff}, \tag{1.2}$$

where V_v is the normal velocity of Γ, ∇_Γ is the surface gradient, c is the surface concentration of gold, c_b is the bulk concentration of gold, J_{diss} is the rate of dissolution and J_{diff} is the diffusive surface flux. The notation $\dot{c}$ is used for the evolving surface material derivative. The rate of dissolution depends on a surface concentration dependent etching rate $v_0(c)$ and the mean curvature of the surface, H, so that

$$J_{diss} = v_0(c)(1 - \delta H).$$

The diffusive flux is of Cahn-Hilliard type which allows up-hill diffusion and leads to phase separation so that

$$J_{diff} = -b(c)\nabla_\Gamma w, w = -\gamma \Delta_\Gamma c + \Psi'(c)$$

where w is the chemical potential, $b(c)$ is a mobility, and Ψ is a double well free energy. In Section 2 the model is described in detail.

Thus we are led to the study of the coupled system of forced mean curvature flow for an evolving surface with the forcing depending on the solution of the Cahn-Hilliard equation. This is a highly nonlinear system.

In this paper we present a novel computational method for solving a fourth order nonlinear diffusion equation on a complex evolving hypersurface. We choose to solve numerically using an evolving triangulation. The surface evolution by forced mean curvature flow is treated by the method of [10]. The conservation law for the concentration is then handled in a natural way using the evolving surface finite element method from [5–7]. During the simulation of dissolution the surface develops a highly complex morphology and the solution of the diffusion equation exhibits transition layers. Thus it is necessary to retriangulate in order both to preserve quasi-regular triangulations and to adapt the grid to the concentration profile. We refer to [4,18,20] for previous works on spinodal decomposition and phase ordering on surfaces.

In the numerical experiments we observe results in agreement to results in [15] and to the Monte-Carlo-simulations in [14]. During the dissolution the surface area of the alloy exposed to electrolyte increases and is decomposed into three subregions: the gold rich portion, $\Gamma_g(t)$, the gold poor region, $\Gamma_e(t)$, and the interfacial transition layer, $\Gamma_l(t)$. The portion, $\Gamma_g(t)$, which is almost completely covered by gold stops moving due to the vanishing of the etching rate, $v_0(c)$, in the pure phase. On the other hand it continues to increase in size as etching takes place in $\Gamma_e(t)$ exposing gold which diffuses uphill towards $\Gamma_g(t)$ leading to an evolving interfacial layer which increases in length and complexity. Short time simulations reveal spinodal decomposition patterns similar to those for flat surfaces and increasing complexity of the surface morphology. We perform longer time simulations on small parts of the surface. We observe that the complexity of the surface increases when the etching rate is sufficiently high suggesting the formation of porosity. This effect does not depend solely on the concentration distribution in the bulk, but can even be observed when the bulk concentration is constant. There are two mechanisms for this effect. One is the nucleation of new regions covered by gold inside the portion, $\Gamma_e(t)$, which is not yet covered in gold. These form new islands of $\Gamma_g(t)$ separated from $\Gamma_e(t)$ by the transition layer $\Gamma_l(t)$. The other is caused by the diffusion of gold in $\Gamma_e(t)$ which accumulates inhomogeneously at $\Gamma_l(t)$.

The contributions of this paper lie in the development of a computational methodology for the simulation of nonlinear equations on (and coupled with) complicated moving surfaces and in the numerical simulations which show that the model describes the formation of complex morphology leading to nanoporosity during surface dissolution.

1.1. Notation

Suppose Γ is a smooth hypersurface in $\mathbb{R}^3$ with normal ν. For a function η defined in a neighbourhood of Γ we denote the tangential gradient on Γ by

$$\nabla_\Gamma \eta = \nabla \eta - (\nabla \eta \cdot \nu)\nu, \tag{1.3}$$

where $x \cdot y$ denotes the Euclidean scalar product and ∇ is the usual gradient on $\mathbb{R}^3$. The tangential gradient only depends on the values of η on Γ. The Laplace–Beltrami-Operator is the tangential divergence of the tangential gradient:

$$\Delta_\Gamma \eta = \nabla_\Gamma \cdot \nabla_\Gamma \eta. \tag{1.4}$$

Let μ be the conormal vector, i.e. the outward pointing normal of $\partial\Gamma$ tangential to Γ. The formula for integration by parts is given by

$$\int_\Gamma \nabla_\Gamma \eta = \int_\Gamma \eta H \nu + \int_{\partial\Gamma} \eta \mu, \tag{1.5}$$

where H is the mean curvature of Γ, defined by $H = -\nabla_\Gamma \cdot \nu$. It is convenient to observe that

$$H\nu = -\Delta_\Gamma \mathrm{id}, \tag{1.6}$$

where $\mathrm{id}(x) = x$ for $x \in \mathbb{R}^3$. The material derivative of a scalar function f defined on a neighbourhood of a time dependent hypersurface $\Gamma(t)$ will be denoted by a dot and is given by

$$\dot{f} = \frac{\partial f}{\partial t} + V \cdot \nabla f, \tag{1.7}$$

where V is the velocity of the surface. We are also going to need the following formula for the differentiation of a parameter-dependent surface integral, see [6] for example,

$$\frac{\mathrm{d}}{\mathrm{d}t}\int_\Gamma f = \int_\Gamma (\dot f + f\nabla_\Gamma \cdot V). \tag{1.8}$$

In our model we will consider a periodic setting. We call a two dimensional surface Σ periodic if there is a diffeomorphism $\Phi : \mathbb{R}^2 \to \Sigma$ that satisfies $\Phi(x + le_1 + ke_2) = \Phi(x) + l\tau_1 + k\tau_2$ for all $l, k \in \mathbb{Z}$ and $x \in \mathbb{R}^2$. Here e_1 and e_2 are the unit vectors in $\mathbb{R}^2$ and $\tau_1, \tau_2 \in \mathbb{R}^3$. Γ will be the image of the unit square $\Gamma = \Phi((0,1)\times(0,1))$. A periodic function η on Γ satisfies $\eta(x) = \eta(x + l\tau_1 + k\tau_2)$ for all $l, k \in \mathbb{Z}$ and $x \in \Gamma$. Formula (1.5) simplifies for a periodic function η:

$$\int_\Gamma \nabla_\Gamma \eta = \int_\Gamma \eta H v. \tag{1.9}$$

1.2. Outline of paper

The mathematical model is formulated in Section 2. The approximation by the evolving surface finite element method is described in Section 3. The method is based on deforming triangulated surfaces. In order to avoid degenerate meshes it is necessary to remesh during the computations. This method is based on conformal parametrization and is described in Section 4. Numerical experiments are described in Section 5. There is a final concluding section.

2. Mathematical model

2.1. The equations

We consider the etching of a binary alloy occupying the bulk region $\Omega(t) \subset \mathbb{R}^3$ by the action of an electrolyte on the upper two dimensional surface $\Gamma(t)$ of $\Omega(t)$. To fix the discussion we consider a silver–gold alloy in an electrolyte for which gold is inert and the silver dissolves. The dissolution occurs at the surface of the alloy and as the silver is etched away a mono-layer of gold accumulates on the surface and locally inhibits further dissolution. We set $0 \leqslant c \leqslant 1$ to denote the surface molar fraction of gold. Denoting by $\mathcal{A}_\mathrm{v}$ the atomic volume, we have that $(\mathcal{A}_\mathrm{v})^{\frac{1}{3}}\int_{\Gamma(t)} c$ is the volume of gold on the surface. Similarly in the bulk we set c_b between 0 and 1 to denote the molar fraction and it follows that the total volume of gold in the system is $\int_{\Omega(t)} c_\mathrm{b} + (\mathcal{A}_\mathrm{v})^{\frac{1}{3}}\int_{\Gamma(t)} c$. We suppose that there is no diffusion in the bulk so c_b is time independent. The etching process on the surface $\Gamma(t)$ is assumed to take place in the normal direction according to the surface evolution equation

$$V = v_0(c)(1 - \delta H)\nu. \tag{2.1}$$

The normal ν is pointing into the bulk domain Ω. The prescribed etching rate function v_0 depends on the concentration of gold on the surface. We assume that v_0 is monotonically decreasing and satisfies $v_0(1) = 0$ so that the etching process stops in areas where the surface is completely covered by gold. During the evolution of the surface gold atoms are picked up from the bulk and agglomerate on the surface. For an arbitrary portion $\mathcal{M}(t)$ of the surface the rate of change of the surface volume of gold due to the motion of $\mathcal{M}(t)$ with the velocity V is given by $\int_{\mathcal{M}(t)} c_\mathrm{b} V \cdot \nu$. Denoting $c_\mathrm{b}/(\mathcal{A}_\mathrm{v})^{\frac{1}{3}}$ by c_0 and taking into account the tangential flux q of the motion of gold adatoms on the surface, we arrive at the following conservation law:

$$\frac{\mathrm{d}}{\mathrm{d}t}\int_{\mathcal{M}(t)} c = -\int_{\partial\mathcal{M}(t)} q\cdot\mu + \int_{\mathcal{M}(t)} c_0 V\cdot\nu.$$

With the formula for integration by parts (1.5), we obtain

$$\int_{\partial\mathcal{M}(t)} q\cdot\mu = \int_{\mathcal{M}(t)} \nabla_\Gamma \cdot q.$$

and the Leibniz formula (1.8) yields

$$\frac{\mathrm{d}}{\mathrm{d}t}\int_{\mathcal{M}(t)} c = \int_{\mathcal{M}(t)} \dot c + c\nabla_\Gamma \cdot V$$

so that

$$\int_{\mathcal{M}(t)} \dot c + c\nabla_\Gamma\cdot V + \nabla_\Gamma \cdot q - c_0 V\cdot\nu = 0.$$

Since we assume that this equation holds for arbitrary portions $\mathcal{M}(t)$ of $\Gamma(t)$, we obtain the pointwise conservation equation

$$\dot c + c\nabla_\Gamma\cdot V + \nabla_\Gamma\cdot q - c_0 V\cdot\nu = 0 \quad \text{on} \quad \Gamma. \tag{2.2}$$

The model assumes that on the surface there is a diffusive tangential flux of gold adatoms so that we choose

$$q = -b(c)\nabla_\Gamma w, \tag{2.3}$$

with the mobility,

$$b(c) = 4Mc(1-c), \quad \text{with} \quad M \in \mathbb{R}$$

and the chemical potential w. The model assumes a regular solution homogeneous free energy

$$\Psi(c) = \frac{\theta_{cr}}{2}c(1-c) + \frac{\theta}{4}(c\log(c) + (1-c)\log(1-c)), \tag{2.4}$$

for the binary mixture of gold and electrolyte adatoms in the mono-layer and a Cahn-Hilliard surface free energy functional

$$E(c) = \int_{\Gamma(t)} \left(\frac{\gamma}{2} \mid \nabla_\Gamma c\mid^2 + \Psi(c)\right), \tag{2.5}$$

where γ is a gradient energy coefficient. Thus the chemical potential w is given as

$$w = -\gamma\Delta_\Gamma c + \Psi'(c). \tag{2.6}$$

In the expression for the regular solution free energy the parameter θ is proportional to the absolute temperature. If θ is lower than the critical value θ_{cr}, then Ψ takes a double well form with equal minima at values c_g and $1-c_g$. In the case of a stationary surface phase separation occurs into two regions corresponding to the electrolyte rich phase where c is approximately $1-c_g$ and the gold rich phase where c is approximately c_g. Those regions are separated by transition interfaces whose thickness is $O(\gamma^{\frac{1}{2}})$.

Thus we obtain the following complete set of equations:

Problem 2.1. Find a periodic evolving surface $\Gamma(t), t \in (0,T)$ and a periodic function $c : \bigcup_{t\in[0,T]}\Gamma(t)\times\{t\}\mapsto\mathbb{R}$, such that the surface moves with the velocity

$$V = v_0(c)(1-\delta H)v, \tag{2.7}$$

and c solves the equation

$$\dot{c} + \nabla_\Gamma\cdot(b(c)\nabla_\Gamma(\gamma\Delta_\Gamma c - \Psi'(c))) + c\nabla_\Gamma\cdot V = c_0 V\cdot v, \tag{2.8}$$

with the initial values

$$c(\cdot,0) = c_i(\cdot) \quad \text{and} \quad \Gamma(0) = \Gamma_0.$$

We want to remark that we have formulated the equations in terms of the concentration of gold. Often the Cahn-Hilliard equations are given in terms of the difference of concentration of the two phases. While this change of variables in the Cahn-Hilliard equation can be compensated by a corresponding change of coefficients in the equation, Eq. (2.2) would take quite a different form since in our case only one quantity (the gold) is conserved, while the other (the electrolyte) is not. The conservation of gold here reads

$$\frac{\mathrm{d}}{\mathrm{d}t}\left(\int_{\Gamma(t)} c + \int_{\Omega(t)} c_0\right) = 0.$$

2.2. Variational form

The geometric PDE (2.1) degenerates when the concentration on the surface approaches 1. Physically this corresponds to the surface stopping to move in portions where it is completely covered by gold. In order to maintain this effect in the numerical simulations we found it convenient to rewrite Eq. (2.1) with the etching rate $v_0(c)$ in the denominator of the left hand side. While this might not be the best way to treat the continuous problem, it works fine for the discretized problem since the computed concentration is smaller than 1 in that case. By multiplying with an arbitrary test function $\varphi : \Gamma(t)\to\mathbb{R}^3$ and using (1.9) we arrive at the variational form

$$\int_{\Gamma(t)} \frac{1}{v_0(c)} V\cdot\varphi + \delta\int_{\Gamma(t)} \nabla_{\Gamma(t)}\mathrm{id} : \nabla_{\Gamma(t)}\varphi = \int_{\Gamma(t)} v\cdot\varphi, \tag{2.9}$$

where for 3×3 matrices A, B we set $A : B = tr(AB^\top)$.

The Cahn-Hilliard Eq. (2.8) is split into two second order problems for the concentration c and the chemical potential w. By integrating with arbitrary test functions η, ψ and using the Leibniz formula (1.8), we arrive at

$$\frac{\mathrm{d}}{\mathrm{d}t}\int_{\Gamma(t)} c\eta + \int_{\Gamma(t)} b(c)\nabla_{\Gamma(t)}w\cdot\nabla_{\Gamma(t)}\eta - \int_{\Gamma(t)} c_0 V\cdot v\eta = \int_{\Gamma(t)} c\dot{\eta} \tag{2.10}$$

$$\int_{\Gamma(t)} w\psi - \gamma\int_{\Gamma(t)} \nabla_{\Gamma(t)}c\cdot\nabla_{\Gamma(t)}\psi - \int_{\Gamma(t)} \Psi'(c)\psi = 0. \tag{2.11}$$

3. Approximation by finite elements

3.1. Semi-discrete approximation

The numerical scheme is based on solving over a time dependent Lipschitz periodic surface, $\Sigma_h(t)$ with a unit cell $\Gamma_h(t)$, composed of a union of triangles. This means that for each t there is a piece-wise linear Lipschitz mapping $\Phi_t^h : \mathbb{R}^2 \to \Sigma_h$ that satisfies $\Phi_t^h(x + le_1 + ke_2) = \Phi_t^h(x) + l\tau_1 + k\tau_2$ for all $l, k \in \mathbb{Z}$ and $x \in \mathbb{R}^2$ where e_1 and e_2 are the unit vectors in $\mathbb{R}^2$ and $\tau_1, \tau_2 \in \mathbb{R}^3$ are given. The image of the unit square is denoted by $\Gamma_h(t)$ which is a triangulated surface composed of triangles in the triangulation $\mathcal{T}_h(t)$. The vertices interpolate Φ_t^h in such a way that the boundary of $\Gamma_h(t)$ is composed of edges of triangles and there is a vertex at $\Phi_t^h((0,0))$. It follows that $\Gamma_h(t)$ is the image under Φ_t^h of a triangulation of the unit square $[0,1] \times [0,1]$ whose vertices on $(1,\cdot)$ and $(\cdot,1)$ are translates of vertices on $(0,\cdot)$ and $(\cdot,0)$.

Translations by multiples of τ_1 and τ_2 define an equivalence relation on the surface $\Sigma_h(t)$. Two vertices $X, Y \in \Sigma_h(t)$ are called equivalent, $X \sim Y$ if there are $k, l \in \mathbb{Z}$ such that their coordinates satisfy $X = Y + k\tau_1 + l\tau_2$. The set of equivalence classes will be called $\mathcal{V}$ and let $\tilde{x}_j$, $j = 1, \ldots, N$ with $N = |\mathcal{V}|$ be an enumeration of the equivalence classes. This equivalence relation and the relation of the coordinates are preserved during the evolution of the surface. Observe that if a vertex is situated on the boundary of $\Gamma_h(t)$, then all equivalent points on the boundary are also vertices of the triangulation.

On the time dependent triangular surface $\Gamma_h(t)$ we set

$$S_h(\Gamma_h(t), \mathbb{R}^n) = \{\chi \in C^0(\Gamma_h(t), \mathbb{R}^n) \mid \chi|_e \quad \text{is linear affine for each e} \quad \in \mathcal{T}_h(t)\}, \tag{3.1}$$

and

$$S_h^{\mathrm{per}}(\Gamma_h(t), \mathbb{R}^n) = \{\chi \in S_h(\Gamma_h(t), \mathbb{R}^n) \mid \chi(X) = \chi(Y) \quad \text{if} \quad X \sim Y\}. \tag{3.2}$$

As an abbreviation we will write $S_h^{\mathrm{per}}(\Gamma_h(t)) = S_h^{\mathrm{per}}(\Gamma_h(t), \mathbb{R})$. The dimension of this space is the number of equivalence classes of vertices. A basis is given by the nodal basis functions defined by

$$\phi_j(x_i) = \begin{cases} 1 & \text{if} \quad x_i \in \tilde{x}_j \\ 0 & \text{else} \end{cases} \quad \text{for} \quad j = 1, \ldots, N. \tag{3.3}$$

A crucial fact concerning these basis functions is the transport property [6]:

$$\dot{\phi}_i = 0 \quad \text{for} \quad i = 1, \ldots, N. \tag{3.4}$$

We use mass lumping for L^2 inner products on the discrete surface Γ_h. This was applied to the cartesian Cahn-Hilliard equation, see [1,2], in order to make the resulting equations easier to solve. We also use it for the additional term accounting for the accumulation of gold on the surface and for the geometric motion. This assures that a vertex stops moving and no additional gold from the bulk is agglomerated there if the concentration is very close to 1.

For functions φ, χ that are continuous on each triangle $T \in \mathcal{T}_h$, we set

$$(\varphi, \chi)_{\Gamma_h}^h = \sum_{j \in \mathcal{V}} \sum_{T \in \mathcal{T}_h, j \in \partial T} \lim_{x \to x_j, x \in T} \varphi(x)\chi(x) \int_T \phi_j, \tag{3.5}$$

for functions that are continuous on Γ_h this reduces to

$$(\varphi, \chi)_{\Gamma_h}^h = \sum_{j \in \mathcal{V}} m_j \varphi(x_j)\chi(x_j) \quad \text{with} \quad m_j = \int_{\Gamma_h} \phi_j. \tag{3.6}$$

The initial given surface is defined by an interpolation of $\Phi_0((0,1) \times (0,1))$ where Φ_0 is prescribed.

Problem 3.1. For $t \in [0,T]$ find discrete surfaces $\Gamma_h(t)$ and $C, W : [0,T] \to S_h^{\mathrm{per}}(\Gamma_h(t))$ such that for all $j = 1, \ldots, N$:

$$\frac{\mathrm{d}}{\mathrm{d}t}(C, \phi_j(t))_{\Gamma_h(t)}^h = -\int_{\Gamma_h(t)} b(C)\nabla_{\Gamma_h(t)} W \nabla_{\Gamma_h(t)} \phi_j(t) + (c_0 V \cdot \nu, \phi_j(t))_{\Gamma_h(t)}^h \tag{3.7}$$

$$(W, \phi_j(t))_{\Gamma_h(t)}^h = \gamma \int_{\Gamma_h(t)} \nabla_{\Gamma_h(t)} C \nabla_{\Gamma_h(t)} \phi_j(t) + (\Psi'(C), \phi_j(t))_{\Gamma_h(t)}^h, \tag{3.8}$$

and such that

$$\left(X_t, \frac{1}{\nu_0(C)}\eta\right)_{\Gamma_h(t)}^h = \int_{\Gamma_h(t)} v \cdot \eta - \delta \int_{\Gamma_h(t)} \nabla_{\Gamma_h(t)} \mathrm{id} \nabla_{\Gamma_h(t)} \eta \quad \forall \eta \in S_h^{\mathrm{per}}(\Gamma_h(t), \mathbb{R}^3), \tag{3.9}$$

where the coordinates of the vertex x_j on $\Gamma_h(t)$ are given by $X(t, x_j)$

3.2. Fully discrete scheme

In the obvious way we consider triangulated surfaces Γ_h^m associated with the times $t^m = m\tau$ where $\tau > 0$ is the time step. Given Γ_h^m and C_h^m and $W_h^m \in S_h^{\mathrm{per}}(\Gamma_h^m)$ we calculate Y_h^{m+1}, C_h^{m+1} and $W_h^{m+1} \in S_h^{\mathrm{per}}(\Gamma_h^m)$. Here Y_h^{m+1}/τ is an approximation to the surface velocity and Γ_h^{m+1} is defined as the triangulated surface whose vertices have coordinates $X_j^{m+1}(x_j) = X^m(x_j) + Y^{m+1}(x_j)$.

The discretization in time is carried out in a semi-implicit way. First the new surface Γ_h^{m+1} is computed using the concentration from the previous time step to compute the dissolution rate v_0. The new triangulated surface is computed with an implicit discretization of the surface Laplacian over the previous surface as explained in [3,10]. This yields a linear system of equations for the surface evolution.

Again for the Cahn-Hilliard equation we use a semi-implicit-scheme. The equation is treated on the newly computed surface Γ_h^{m+1}. The mobility is evaluated using the concentration from the previous time step while the nonlinear logarithmic term is treated implicitly. This has the advantage that the numerical solution of the discrete system has the property that the concentration takes only values in the open interval $(0,1)$, see [1,2]. The time derivative in Eq. (3.7) is discretized as

$$\frac{1}{\tau}((C^{m+1},\phi_j^{m+1})_{m+1}^h-(C^m,\phi_j^m)_m^h), \tag{3.10}$$

where $(\cdot,\cdot)_m^h=(\cdot,\cdot)_{\Gamma_h^m}^h$ while all other integrals are computed on the surface calculated in the current timestep. In order to define the explicitly discretized mobility on the new surface, we define for given Γ_h^{m+1}, Γ_h^m

$$C^{m,+}=\sum_{j=1}^N C_j^m\phi_j^{m+1}. \tag{3.11}$$

Here C_j^m are the values of the finite element function $C^m\in S_h^{\mathrm{per}}(\Gamma_h^m)$ at the vertices, i.e. $C^m=\sum_{j=1}^N C_j^m\phi_j^m$.

Algorithm 1 (*Fully discrete scheme*). Let $\Gamma_h^m, C^m\in S_h^{\mathrm{per}}(\Gamma_h^m)$ be given

- Find the solution $Y^{m+1}\in S_h^{\mathrm{per}}(\Gamma_h^m,\mathbb{R}^{\mathbb{R}^3})$ of the linear equation

$$\frac{1}{\tau}(Y^{m+1},\frac{1}{v_0(C)}\eta)_m^h+\delta\int_{\Gamma_h^m}\nabla_{\Gamma_h^m}Y^{m+1}\nabla_{\Gamma_h^m}\eta \tag{3.12}$$

$$=-\delta\int_{\Gamma_h^m}\nabla_{\Gamma_h^m}X^m\nabla_{\Gamma_h^m}\eta+\int_{\Gamma_h^m}v^m\eta\quad\forall\eta\in S_h^{\mathrm{per}}(\Gamma_h^m,\mathbb{R}^3). \tag{3.13}$$

- Γ_h^{m+1} is defined by the new coordinates of the vertices $X_j^{m+1}(x_j)=X^m(x_j)+Y^{m+1}(x_j)$.
- Find C^{m+1} and W^{m+1} by solving the linear equations for all $j=1,\dots,N$:

$$\frac{1}{\tau}(C^{m+1},\phi_j^{m+1})_{m+1}^h+\int_{\Gamma_h^{m+1}}\mathrm{b}(C^{m,+})\nabla_{\Gamma_h^{m+1}}W^{m+1}\nabla_{\Gamma_h^{m+1}}\phi_j^{m+1}$$

$$=\frac{1}{\tau}(C^m+c_0v^m\cdot Y^{m+1},\phi_j^m)_m^h \tag{3.14}$$

$$(W^{m+1},\phi_j^{m+1})_{m+1}^h$$

$$=\gamma\int_{\Gamma_h^{m+1}}\nabla_{\Gamma_h^{m+1}}C^{m+1}\nabla_{\Gamma_h^{m+1}}\phi_j^{m+1}+(\Psi'(C^{m+1})),\phi_j^{m+1})_{m+1}^h. \tag{3.15}$$

The equation for the surface evolution is linear with a positive definite matrix, and can easily be solved by a conjugate gradient method.

In order to analyze the coupled equations for the concentration and chemical potential we write them in matrix form. We define the stiffness matrix S, the mobility weightened stiffness matrix B and the diagonal mass matrix M by

$$S_{ij}^{m+1}=\int_{\Gamma_h^{m+1}}\nabla_{\Gamma_h^{m+1}}\phi_i^{m+1}\nabla_{\Gamma_h^{m+1}}\phi_j^{m+1}$$

$$B_{ij}^{m+1}=\int_{\Gamma_h^{m+1}}\mathrm{b}(C^{m,+})\nabla_{\Gamma_h^{m+1}}\phi_i^{m+1}\nabla_{\Gamma_h^{m+1}}\phi_j^{m+1}$$

$$M_{ij}^{m+1}=\int_{\Gamma_h^{m+1}}\phi_i^{m+1}\delta_{ij}.$$

To write the system to be solved in matrix form, we define $\mathbf{c^{m+1}}\in\mathbb{R}^N$ by $(\mathbf{c^{m+1}})_i=C^{m+1}(\tilde{x}_i)$ and analogously for $\mathbf{w^{m+1}}$. For the purpose of analyzing the algorithm we define $\tilde{\mathbf{b}}^{\mathbf{m+1}}\in\mathbb{R}^N$ by

$$\tilde{\mathbf{b}}_i^{\mathbf{m+1}}:=\frac{1}{M_{ii}^{m+1}}\left(M_{ii}^mC_i^m+c_0(v^m\cdot Y^{m+1},\phi_i^m)_m^h\right). \tag{3.16}$$

In this notation Eqs. (3.14) and (3.15) take the form

$$M^{m+1}\mathbf{c^{m+1}}=-\tau B^{m+1}\mathbf{w^{m+1}}+M^{m+1}\tilde{\mathbf{b}}^{\mathbf{m+1}} \tag{3.17}$$

$$M^{m+1}\mathbf{w^{m+1}}=\gamma S^{m+1}\mathbf{c^{m+1}}-\theta_{\mathrm{cr}}M^{m+1}\left(\mathbf{c^{m+1}}-\frac{1}{2}\right)+M^{m+1}\psi(\mathbf{c^{m+1}}), \tag{3.18}$$

where $\psi(\mathbf{x})_i = \frac{\theta}{4}\log\left(\frac{\mathbf{x}_i}{1-\mathbf{x}_i}\right)$.

3.3. Solving the algebraic system

In order to present an algorithm for solving the algebraic system we define $G^{m+1}: V^{m+1} \to V^{m+1}$ by

$$B^{m+1}G^{m+1}\mathbf{x} = M^{m+1}\mathbf{x} \quad \text{and} \quad \mathbf{1}^\top M^{m+1}G^{m+1}\mathbf{x} = 0, \tag{3.19}$$

where $V^{m+1} = \{x \in \mathbb{R}^N, \mathbf{1}^\top M^{m+1}x = 0\}$ and $\mathbf{1} \in \mathbb{R}^N$ is the vector whose components are all equal to one. This operator can be used to eliminate $\mathbf{w^{m+1}}$ and we get a single equation for $\mathbf{c^{m+1}}$:

$$\mathcal{A}(\mathbf{c^{m+1}}) + \mathcal{B}(\mathbf{c^{m+1}}) - \lambda\mathbf{1} = 0. \tag{3.20}$$

Here

$$\mathcal{A}: (0,1)^N \to \mathbb{R}^N$$
$$\mathcal{A}(\mathbf{x}) = \psi(\mathbf{x})$$
$$\mathcal{B}: D(\mathcal{B}) \to V^m$$
$$\mathcal{B}(\mathbf{x}) = G^{m+1}\left(\frac{\mathbf{x}-\tilde{\mathbf{b}}}{\tau}\right) + \gamma(M^{m+1})^{-1}S^{m+1}\mathbf{x} - \theta_{\mathrm{cr}}\mathbf{x},$$

where $D(\mathcal{B}) = \{x \in \mathbb{R}^N \mid \mathbf{1}^\top M^{m+1}x = \mathbf{1}^\top M^{m+1}\tilde{b}\}$ and λ is given by $\lambda = \frac{1}{|\Gamma_h^{m+1}|}\mathbf{1}^\top M^{m+1}\psi(\mathbf{c^{m+1}})$. While $\mathcal{A}$ is a strictly monotone operator and $\mathcal{B}$ is a coercive operator with respect to the scalar product induced by the matrix M^{m+1} if $\tau < \frac{4\gamma}{\theta_{\mathrm{cr}}^2}$. To solve this equation, we use the operator splitting scheme (see [17]), which has been applied to the Cahn-Hilliard equation in the plane with a constant mobility in [2,12]. In [1] a variant of this algorithm is applied for solving the Cahn-Hilliard equation with a degenerate mobility. But the effectiveness of this algorithm depends heavily on using direct methods for solving the discrete Poisson equation, which can not be applied in the case of a triangulated surface. So we adapt the iteration in [2]. The operator splitting scheme yields the iteration

$$\mathbf{c}^{\mathbf{m+1}}_{\mathbf{j}+\frac{1}{2}} + \mu\mathcal{A}\left(\mathbf{c}^{\mathbf{m+1}}_{\mathbf{j}+\frac{1}{2}}\right) = \mathbf{c}^{\mathbf{m+1}}_{j} - \mu\mathcal{B}(\mathbf{c}^{\mathbf{m+1}}_{\mathbf{j}}) + \mu\lambda_j\mathbf{1} \tag{3.21}$$

$$\mathbf{c}^{\mathbf{m+1}}_{\mathbf{j}+1} + \mu\mathcal{B}(\mathbf{c}^{\mathbf{m+1}}_{\mathbf{j}+1}) - \mu\lambda_{j+1}\mathbf{1} = \mathbf{c}^{\mathbf{m+1}}_{\mathbf{j}+\frac{1}{2}} - \mu\mathcal{A}\left(\mathbf{c}^{\mathbf{m+1}}_{\mathbf{j}+\frac{1}{2}}\right). \tag{3.22}$$

While this iterative scheme converges, the number of iterations needed to obtain an approximate solution for our case of a degenerate mobility and small values of $\frac{\theta}{\theta_{\mathrm{cr}}}$ is rather high. Changing Eq. (3.22) to

$$\mathbf{c}^{\mathbf{m+1}}_{\mathbf{j}+1} + \mu\mathcal{B}(\mathbf{c}^{\mathbf{m+1}}_{\mathbf{j}+1}) + \mu\phi_\epsilon\left(\mathbf{c}^{\mathbf{m+1}}_{\mathbf{j}+\frac{1}{2}}\right)\mathbf{c}^{\mathbf{m+1}}_{\mathbf{j}+1} - \mu\lambda_{\mathbf{j}+1}\mathbf{1} = \mathbf{c}^{\mathbf{m+1}}_{\mathbf{j}+\frac{1}{2}} - \mu\mathcal{A}\left(\mathbf{c}^{\mathbf{m+1}}_{\mathbf{j}+\frac{1}{2}}\right) + \mu\phi_\epsilon\left(\mathbf{c}^{\mathbf{m+1}}_{\mathbf{j}+\frac{1}{2}}\right)\mathbf{c}^{\mathbf{m+1}}_{\mathbf{j}+\frac{1}{2}}, \tag{3.23}$$

resulted in a significant decrease of the number of iteration. Here $\phi_\epsilon(\boldsymbol{x})$ is the regularized derivative of ψ, given by

$$\phi_\epsilon(\boldsymbol{x})_{ij} = \begin{cases} \frac{\theta\delta_{ij}}{4\boldsymbol{x}_i(1-\boldsymbol{x}_i)} & \text{if} \quad \varepsilon \leqslant \boldsymbol{x}_i \leqslant 1-\varepsilon \\ \frac{\theta\delta_{ij}}{4\varepsilon(1-\varepsilon)} & \text{if} \quad \boldsymbol{x}_i < \varepsilon \quad \text{or} \quad 1-\varepsilon < \boldsymbol{x}_i \end{cases}. \tag{3.24}$$

The regularization is needed because otherwise the iterative procedure in general does not converge. A heuristic choice for ε, which resulted experimentally in convergence and produced the solution after relatively few iterations was to take ε to be the maximum norm of the change of $\mathbf{c^m_j}$ from one iteration step to the next.

4. Mesh smoothing

The motion of the surface leads to variations in the shape of the triangles which may be undesirable. First, the relative size of the triangles changes as the surface deforms and increases in area. We account for this by coarsening and refining at each time step according to two criteria. In order to achieve a homogeneous triangulation with respect to the area of the triangles, a triangle is refined as soon as its area exceeds twice the average area of triangles of the initial triangulation. Second, we want to resolve the interface between the gold rich and gold poor phase on the surface. To achieve this, a triangle is refined as soon as the variation of concentration on this triangle exceeds $\frac{1}{10}$, ensuring that there are at least ten triangles across the interface. Finally as the surface deforms the angles of the triangulation degenerate. In contrast to the previous cases this is not addressed at each time step because enhancing this aspect generally involves a more difficult computation which involves relocating vertices on the surface. So we choose an acceptable mesh regularity criterion and then retriangulate the surface completely as soon as it is no longer fulfilled. The chosen criterion is that the minimum angle of the triangulation is larger than $\frac{\pi}{9}$. The basic idea of the method is to compute the approximation of a conformal diffeomorphism into a domain which can easily be triangulated with a regular reference triangulation. Then the inverse of this map is used to lift the reference triangulation onto the surface, resulting in a regular surface mesh. One approach to compute the conformal map using holomorphic one forms is

discussed in [13]. We use a modified approach similar to [11], where it was applied to topological spheres, in order to compute the mapping directly. The periodic surfaces that we have considered in the previous section are topological tori when the equivalence relation is taken into account. We will begin by stating some results concerning conformal maps between tori and then present the algorithm for reparametrizing the surface.

4.1. Conformal mappings for torus domains

A local parametrization $X = X(p_1, p_2) : \mathbb{R}^2 \to \Gamma \subset \mathbb{R}^3$ of a surface is conformal (angle preserving) if

$$\left|\frac{\partial X}{\partial p_1}\right| = \left|\frac{\partial X}{\partial p_2}\right| \quad \text{and} \quad \frac{\partial X}{\partial p_1} \cdot \frac{\partial X}{\partial p_2} = 0. \tag{4.1}$$

These equations are difficult to solve so we use the observation that the inverse of a conformal diffeomorphism is also conformal and seek an inverse conformal map $\Psi : \Gamma \to \mathbb{R}^2$. It is known that Ψ is harmonic and that

$$\nabla_\Gamma \Psi^i \cdot \nabla_\Gamma \Psi^j = \lambda \delta_{ij}, \tag{4.2}$$

for a scalar function λ. It is also known that a manifold diffeomorphic to a torus can be mapped conformally into a flat torus, that is a quotient of $\mathbb{R}^2$ defined by an equivalence relation of the form

$$x \sim y \quad \text{if and only if} \quad x = y + l\tau_1 + k\tau_2 \quad \text{with} \quad k, l \in \mathbb{Z}, \tag{4.3}$$

where it is sufficient to consider the cases $\tau_1 = (1, 0)^\top$ and $\tau_2 = (c, d)^\top$ with $d > 0$. We will denote the flat torus defined by this equivalence relation by $\mathcal{P}_{(c,d)}$. Thus we seek a conformal map Ψ and $\mathcal{P}_{(c,d)}$ such that $\Psi : \Gamma \to \mathcal{P}_{(c,d)}$. In order to achieve this we set $\Psi := A \circ \Phi$ where $\Phi : \Gamma \to \mathcal{Q}$ is a harmonic diffeomorphism into $\mathcal{Q} := \mathcal{P}_{(0,1)}$, where

$$A = \begin{pmatrix} 1 & c \\ 0 & d \end{pmatrix} \quad \text{with} \quad c \in \mathbb{R}, d \in \mathbb{R}^+, \tag{4.4}$$

and $A(\mathcal{Q}) = \mathcal{P}_{(c,d)}$ is chosen so that Ψ is conformal. Note that harmonic mappings from a manifold diffeomorphic to a torus into the quotient spaces within a given homotopy class are unique up to an addition of a constant vector.

Once Φ is determined, we use the conformal conditions (4.2) in order to compute (c, d). Applying the chain rule we get the following relations between the tangential gradients of Ψ and Φ:

$$\nabla_\Gamma \Psi^1 = \nabla_\Gamma \Phi^1 + c \nabla_\Gamma \Phi^2 \quad \text{and} \quad \nabla_\Gamma \Psi^2 = d \nabla_\Gamma \Phi^2. \tag{4.5}$$

Thus taking scalar products of those two equations and using (4.2), we get

$$\begin{aligned} |\nabla_\Gamma \Phi^1|^2 &= \left(1 + \frac{c^2}{d^2}\right)\lambda(x) \\ |\nabla_\Gamma \Phi^2|^2 &= \frac{1}{d^2}\lambda(x) \\ \nabla_\Gamma \Phi^1 \cdot \nabla_\Gamma \Phi^2 &= -\frac{c}{d^2}\lambda(x). \end{aligned}$$

Integrating over Γ and solving for c and d, we arrive at

$$c = -\frac{\int_\Gamma \nabla_\Gamma \Phi^1 \cdot \nabla_\Gamma \Phi^2}{\int_\Gamma |\nabla_\Gamma \Phi^2|^2} \quad \text{and} \quad d = \sqrt{\frac{\int_\Gamma |\nabla_\Gamma \Phi^1|^2}{\int_\Gamma |\nabla_\Gamma \Phi^2|^2} - c^2}. \tag{4.6}$$

4.2. Remeshing

We wish to apply this idea in the context of improving the quality of the surface triangulation. Γ_h is given as a triangulated surface whose vertices are the images of a triangulation of $\mathcal{Q}$. Thus we have the piecewise linear map $U_h : \Gamma_h \to \mathcal{Q}$ which is the inverse of the parametrization of Γ_h. Our goal is to find a map $\Psi_h : \Gamma_h \to \mathcal{P}_{(c_h, d_h)}$ which is an approximation of a conformal map. It then follows that a uniform triangulation $\mathcal{T}_h$ of $\mathcal{P}_{(c_h, d_h)}$ induces a triangulated surface $\tilde{\Gamma}_h$ which approximately maintains the angles of $\mathcal{T}_h$. In order to achieve this we compute a piecewise linear map $\Phi_h \in S_h(\Gamma, \mathbb{R}^2)$ which is discrete harmonic and fixed by

$$\int_{\Gamma_h} \Phi_h = \int_{\Gamma_h} U_h. \tag{4.7}$$

Then (c_h, d_h) can be chosen analogously to Eq. (4.6), so that the map $\Psi_h := A_h \circ \Phi_h$ is approximately conformal. Since we want to use the triangulation on $\mathcal{P}_{(c_h, d_h)}$ to define the triangulation on the surface, the calculated parameters c_h and d_h are changed slightly in order to be able to prescribe a homogeneous triangulation consisting of rectangular triangles on the resulting quotient space. The number of triangles has to be sufficiently high in order to obtain values of c_h and d_h close to the calculated values.

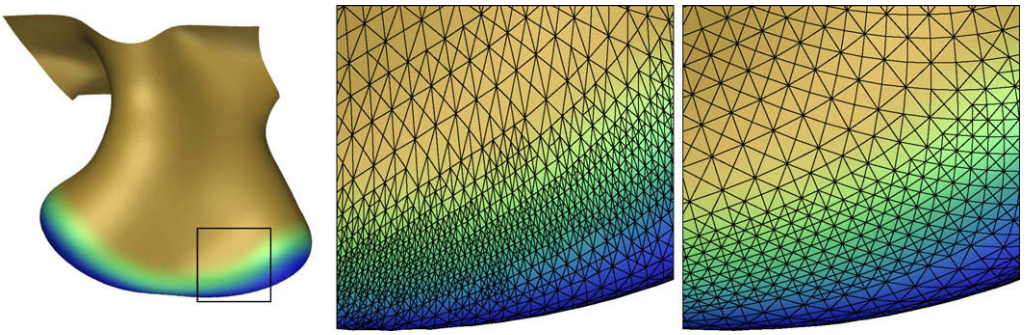

Fig. 1. Remeshed surface, closeup before and after remeshing.

On the other hand it should not be to high since the resulting triangulation is rather inhomogeneous and has to be refined. During the computations we used 1000 triangles for the macro triangulation. Note that it is always possible to use a rectangle for the triangulation, as long as a nonvanishing value of c_h is taken into account by using proper identifications on the boundaries.

The macro triangulation on $\mathcal{P}_{(c_h,d_h)}$ can be used to define a triangulation on the surface by defining the vertices of this triangulation to be the preimages of the vertices on $\mathcal{P}_{(c_h,d_h)}$ with respect to Ψ_h. As mentioned above, the resulting triangulation interpolating Γ_h is rather inhomogeneous and so it has to be refined again according to the criteria mentioned at the beginning of this section. It is important that during this refinement process the coordinates of the new vertices are not taken to be an interpolation of the coordinates of the vertices on the triangle to be refined. Rather the coordinates have to be calculated by finding the preimage of the newly created vertex on $\mathcal{P}_{(c_h,d_h)}$ with respect to Ψ_h.

This leads to the following algorithm.

Algorithm 2 (*Retriangulation of the surface*). Let $U_h : \Gamma_h \to \mathcal{Q}$ be the inverse of a parametrization of the periodic surface over the unit square.

- Compute the approximation $\Phi_h := U_h + \widetilde{\Phi}_h : \Gamma_h \to \mathcal{Q}$ with $\widetilde{\Phi}_h \in S_h^{\mathrm{per}}(\Gamma, \mathbb{R}^2)$ of an harmonic mapping by solving

$$\int_{\Gamma_h} \nabla_{\Gamma_h} \widetilde{\Phi}_h \nabla_{\Gamma_h} \varphi = -\int_{\Gamma_h} \nabla_{\Gamma_h} U_h \nabla_{\Gamma_h} \varphi \quad \forall \varphi \in S_h^{\mathrm{per}}(\Gamma, \mathbb{R}^2) \quad \text{and} \quad \int_{\Gamma_h} \widetilde{\Phi}_h = 0$$

- Find the parameters of the parallelogram by computing

$$c_h = -\frac{\int_{\Gamma_h} \nabla_{\Gamma_h} \Phi_h^1 \cdot \nabla_{\Gamma_h} \Phi_h^2}{\int_{\Gamma_h} |\nabla_{\Gamma_h} \Phi_h^2|^2} \qquad d_h = \sqrt{\frac{\int_{\Gamma_h} |\nabla_{\Gamma_h} \Phi_h^1|^2}{\int_{\Gamma_h} |\nabla_{\Gamma_h} \Phi_h^2|^2} - c_h^2}$$

and change the values slightly in order to allow for a triangulation by rectangular triangles on $\mathcal{P}(c_h, d_h)$. The approximation of the conformal mapping is then given by $\Psi_h := A_h \circ \Phi_h$.

- Find the interpolation of the inverse of the conformal mapping and use it to map a triangulation on the parallelogram onto the surface.
- Refine the resulting surface.

Fig. 1 shows an example of a surface to be retriangulated encountered in computational experiments explained in Section 5.2. The left closeup shows the triangulation before, the right one after retriangulation. Even though the perspective distorts the angles, the improvement can clearly be seen. The mesh before retriangulation seems to be finer across the interface (the green region). This is a consequence of the triangles being distorted in normal direction to the interface by the algorithm for the evolution of the surface. Therefore the second criterion for refining induces smaller triangles for the old mesh in this area.

5. Numerical results

5.1. Numerical tests

We begin by describing the performance of the numerical scheme with respect to the amount of work, the accuracy for a model problem with a smooth solution and the quality of the meshes obtained by using the algorithm of the last section.

5.1.1. Number of iterations for iterative scheme

To test the iterative algorithm presented in Section 3.3 and to find a reasonable value for the parameter μ, we carry out computations on the same system with various values of μ. For these tests we run a simulation with a random concentration on the unit square as initial condition for 100 timesteps. The parameters for the Cahn-Hilliard equation are chosen to be:

$\theta_{cr} = 1, \theta = 0.13$ and $\Gamma = 10^{-3}$, while for the geometric motion in Eq. (2.1), we choose $v_0(c) = e^{-c}(1-c)$ and $\delta = 0.1$. In a first series we use the algorithm of Eqs. (3.21) and (3.22), that is without the additional term introduced in Eq. (3.23). Computations are done for three different values of μ, leading to very high numbers of iteration. Values of μ higher than 1 show even slower convergence. The number of iterations in the computation become high as soon as the values of the concentration come close to the minima of the potential and the singular nature of logarithmic nonlinearity becomes significant.

μ	1	0.1	0.01
Average number of iterations	99,097	24,141	8672

In a second series we use Eq. (3.23) instead of Eq. (3.24) and obtain a significantly lower number of iterations, which turns out to be the better the bigger the chosen value of μ was. Nevertheless with respect to overall computational cost, a value of $\mu = 100$ turns out to be best, since the linear system is more difficult to solve for higher values of μ.

μ	10,000	1000	100	10	1	0.1
Average number of iterations	12.3	12.3	12.9	23.5	115.7	307.9

To further reduce the computational cost per timestep we do not solve the linear system exactly for each step of the iteration but rather reduce the residual by a factor of 100. This has only relatively small consequences on the number of iterations needed but decreases the total computational cost by a factor of about five.

μ	10,000	1000	100	10	1	0.1
Average number of iterations	13.5	14.6	16.9	27.0	117.9	524.5

For the remaining calculations we choose $\mu = 100$ and do not solve the linear system exactly.

5.1.2. Convergence to exact solution for a surface moving with given velocity

In order to test the algorithm for solving the Cahn-Hilliard equation on a moving surface we compute the numerical solution for a surface moving with prescribed velocity. Since the motion of the surface is known, just the second part of Algorithm (1) is used to compute the solution. The surface is given as time dependent graph of a function v over the unit square and the discrete surface is given by the graph of the interpolation at each timestep, using a fixed grid on the unit square. Since no nontrivial solutions for the homogeneous Cahn-Hilliard equation on a moving surface are known analytically, the inhomogeneous equation is solved, the right hand side being computed from the given solution. The parameters are chosen to be $\gamma = 0.01,\ \theta = 0.125$ and $\theta_{cr} = 1$ corresponding to minima in the double well potential at about 10^{-7} and $1 - 10^{-7}$. The graph is given by $v(x) = 0.25\sin(2\pi x_1)\cos(2\pi x_2)\sin\left(\frac{\pi}{2}t\right),\ t \in [0,1]$ and the solution is $c(x) = (1-10^{-6})(0.5 + 0.5\sin(2\pi x_1)\cos(2\pi x_2)t),\ t \in [0,1]$ with periodic boundary conditions. The numerical solution is computed for five triangulations $\mathcal{T}_j,\ j = 0,\dots,4$ created by refining a macro triangulation consisting of four congruent triangles on the unit square $\mathcal{T}2j + 6$ times by bisection. The time step size for the computation on the moving triangulation corresponding to $\mathcal{T}_j$ is given by $\tau_j = 2^{2-j}10^{-2}$, thereby meeting the time step restriction for all values of j. The quantities

$$e_{L^2} = \left(\sum_{n=1}^{N_j} \tau_j \|c(n\tau_j) - \widetilde{C}^n\|^2_{L^2(\Gamma_{n\tau_j})}\right)^{\frac{1}{2}} \quad \text{and} \tag{5.1}$$

$$e_{H^1} = \left(\sum_{n=1}^{N_j} \tau_j \|\nabla_\Gamma(c(n\tau_j) - \widetilde{C}^n)\|^2_{L^2(\Gamma_{n\tau_j})}\right)^{\frac{1}{2}}, \tag{5.2}$$

where N_j is the number of time steps computed for the triangulation $\mathcal{T}_j$ and $\widetilde{C}^n$ is a lift of the discrete solution C^n are computed numerically. These values, the corresponding values of h_{max}, the maximal length of an edge during the evolution of the discrete surface, and the experimental order of convergence are listed in the table.

h_{max}	e_{L^2}	eoc	e_{H^1}	epc
0.0946	0.12632	–	0.8301	–
0.0478	0.07046	0.86	0.4890	0.78
0.0245	0.02826	1.31	0.1353	1.85
0.0123	0.00857	1.721	0.0671	1.01
0.0062	0.00222	1.95	0.0325	1.04
0.0031	0.00051	2.12	0.0164	0.99

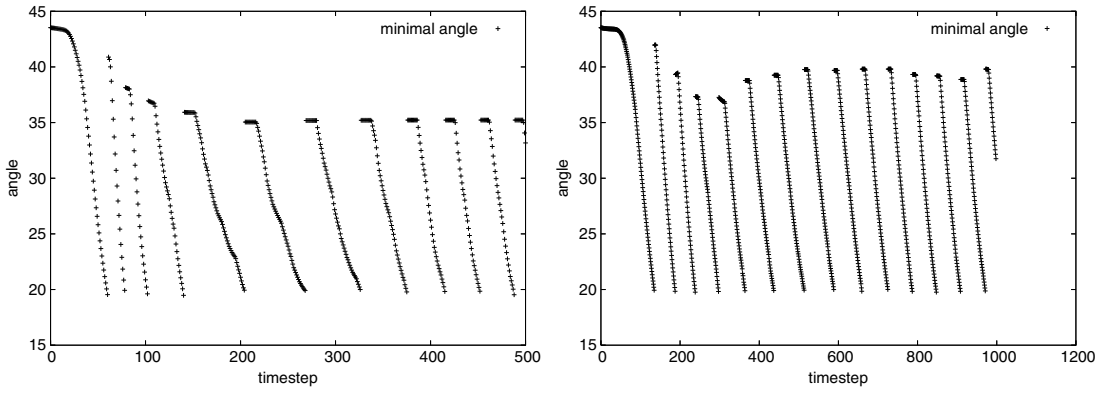

Fig. 2. Minimal angle during the evolution of the surface.

As can be seen in the table the experimental order of convergence approaches a value close to two for the L^2-error, while the order for the H^1-error is close to one.

5.1.3. Test of the remeshing algorithm

In order to show the effectiveness of the mesh smoothing Algorithm (2), we start a simulation with the same initial condition and parameters as in Section 5.1.1, except that we compute 500 timesteps. The left side of Fig. 2 shows the evolution of the minimal angle of all triangles in the triangulation at the corresponding timestep. Since the simulation starts with a uniformly triangulated square, the minimal angle is close to 45° for the first timesteps. As the surface deforms it starts to deteriorate monotonically until an angle of below 20° is reached. At this point the retriangulation algorithm is used and yields an improved triangulation. Even though the optimal angle of 45° is not reached any more, the angle of the newly retriangulated surface is slightly above 35° during the computation.

Refining the triangulation increases the effectiveness of the algorithm. The plot on the right hand side of Fig. 2 shows the results of a simulation with the same parameters but a triangulation refined two times by bisection and half the timestep size. The minimal angle of the newly parametrized surface is larger then on the coarser triangulation.

5.2. Computational experiments

The goal of the numerical experiments is twofold. On the one hand we want to show that the algorithm produces reasonable results for solving the Cahn-Hilliard equation on a surface evolving according to a coupled velocity law. On the other hands the results of the computations are to be compared with experimental results and results of Monte-Carlo-simulations describing the system (compare [14]). In all experiments, the scalar etching rate function in Eq. (2.1) is taken to be of the form $v_0(c) = v_{\max} e^{-c}(1-c)$ and we choose $\delta = 0.1$. Except for absolute scale, variations in the form of the rate function had little effect in computational experiments. The maximal velocity $v_{\max}$ is varied in different experiments. In all subsequent experiments the parameters in the Cahn-Hillard equation are chosen to be $\theta_{\text{cr}} = 1.0$ and $\theta = 0.125$, resulting in minima of the free energy at concentration values about 10^{-7} and $1 - 10^{-7}$ and $\gamma = 10^{-3}$. The mobility is chosen to be $b(c) = 4c(1-c)$ resulting in a degenerate mobility in the pure phases.

5.2.1. Early stages of surface etching and pattern formation

Example 1. In a first experiment we investigate the early stages of etching into a bulk with random variations in the concentration of gold. As initial condition for the geometry, we use the x_1x_2-plane and do the calculations on a square of sidelength 3. The square is triangulated regularly by 2^{15} triangles which is achieved by subdividing an initial triangulation of four rectangular triangles. As timestep size we use $\tau = 10^{-3}$ and we take $v_{\max} = 1.6$. The initial condition for the concentration is chosen as 10^{-7} on the whole square so that in the beginning gold is almost completely absent on the surface. To simulate a random distribution of gold in the bulk, the volume below the square is subdivided into cubes of sidelength 0.1 assigning to each cube a random concentration value between 0 and 24. In the first stages of the simulation, gold from the bulk agglomerates on the surface, which moves with an almost uniform velocity. Because of the inhomogenity of the concentration in the bulk, phase separation starts to occur. This can be seen in the left side of [1]Fig. 3. In this figure the view is from above the surface and yellow denotes portions of the surface almost completely covered by gold, while the gold poor regions are blue. At this stage of the computation, the result looks similar to a simulation of the Cahn-Hilliard equation on a

[1] For interpretation of the references in colour in this figure legend, the reader is referred to the web version of this article.

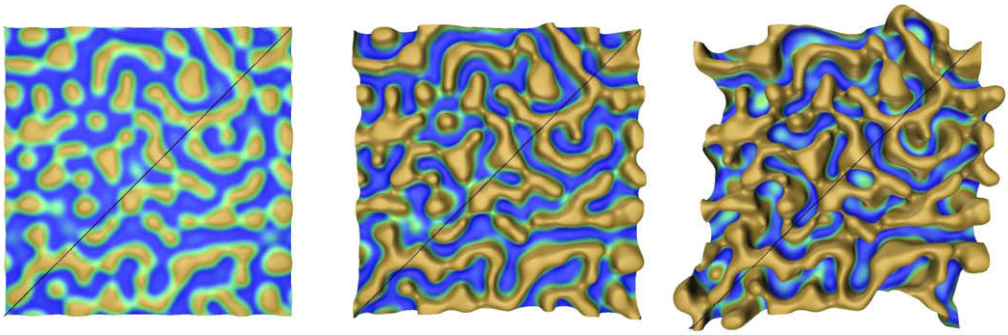

Fig. 3. Simulation on a large square, $t = 0.04$, $t = 0.1$ and $t = 0.2$.

plane. The geometric motion of the surface has little influence, except for providing for a nonvanishing right hand side for the conservation law of gold on the surface, since gold from the bulk is accumulating on the surface. While the concrete appearance of the structure obviously depends on the particular random distribution in the bulk, the lengthscales of the structure depend only on the particular values of the parameters in the equation.

After the phases have separated, etching still continues in the areas with a small concentration of gold, while the motion is negligible in regions covered by gold yielding a maze like structure of the surface. The origins of this shape can still be explained by the initial phase separation which fixed the gold covered regions that proceeded to move into the bulk. So at this stage the simulation does not necessarily show the mechanisms for the emergence of a nanoporous structure. By undercutting the gold rich portion of the surface, the area of the surface that is not covered by gold increases. In the last stages of this simulation new components of the gold rich phase emerge at the bottom of the surface. Additionally the interface separating gold rich and gold poor phases shows no effect of coarsening as for the planar Cahn-Hilliard equation, but instead becomes more complicated. These two effects can be seen as signs that the model shows increasing formation of morphological complexity. We explore them in more detail in the following examples. Note however that due to self-intersections the surface is not embedded at later stages, as can be seen in Fig. 4, where the cross sections along the plane parallel to the x_3-axis and the diagonal of the initial condition are shown. The six figures correspond to equidistant times from $t = 0.04$ to $t = 0.24$.

5.2.2. Pit formation

In the following experiments we investigate the evolution in more detail by focusing on the evolution of a single pit etching into the bulk. As well as having a lower computational complexity this initial configuration has the additional advantage of postponing the unphysical self-intersections to later times. These simulations can be interpreted physically in two ways. They can either be seen as a small portion of the whole bulk at later stages of the etching process, that are separated from the rest by an area completely covered by gold. Because of the vanishing mobility in the gold rich phase, the influence of the rest of the surface on this part is minimal. The other interpretation is the etching of an isolated pit into an otherwise completely passivated bulk.

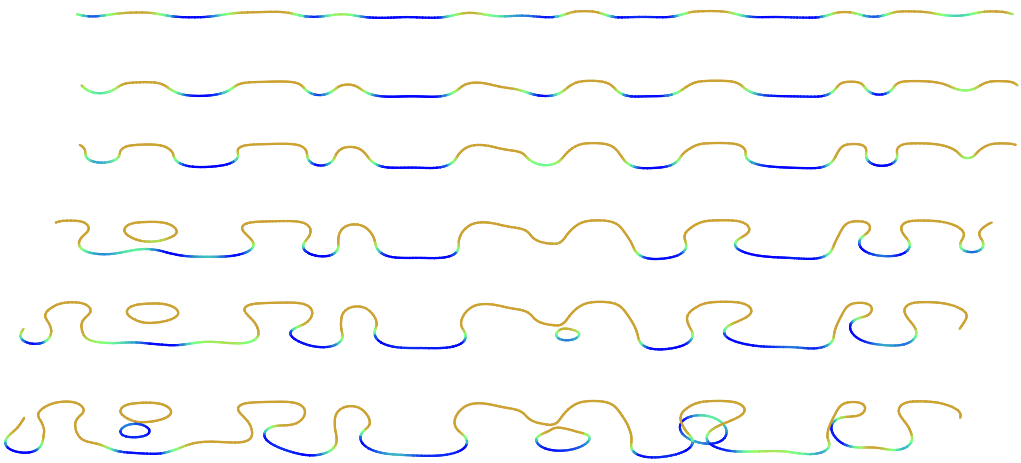

Fig. 4. Simulation on a large square, cross sections along the diagonal for $t = 0.04$–$t = 0.24$.

Example 2. As in experiment 1, we use the x_1x_2-plane as geometric initial condition, but solving on a square of sidelength 0.5 centered at the origin with periodic boundary conditions. The initial discretization consists of 2^{12} triangles and all parameters besides $v_{\max}$ and the concentration in the bulk have the same values as in the computation on the large square.

As a first experiment on the smaller square, we take a smoothed version of $u_0(x) = 1 - \chi_{B_{\frac{1}{5}}}$ as initial condition, where $\chi_{B_{\frac{1}{5}}}$ denotes the characteristic function of the circle with radius 0.2. This can be thought of as a single circular pit where etching is possible, surrounded by an area completely passivated by gold. This is depicted in the left hand side of Fig. 5 which again is a view from above). The concentration in the bulk is taken to be constant with $c_0 = 12$. After a few iterations a circular pit occurs due to etching. After some time the pit undercuts the plane and the region of low concentration of gold increases in size but remains circular in shape. For larger values of $v_{\max}$, a new region covered by gold emerges in the center of the pit while the part not covered by gold has the shape of an annulus and continues to edge into the bulk. This is similar to the result of the analogous Monte-Carlo-simulations in [15]. In contrast, for lower values of $v_{\max}$ we do not observe this effect. The part of the surface not covered by gold rather remains in a circular shape and etches a pit of cylindrical shape into the bulk. This is in accordance with the experimental observation that the formation of nanoporosity greatly increases above a certain etching rate. Fig. 6 shows the result at an earlier stage of the simulation and at a later stage, where the difference in appearance becomes apparent. In order to show the geometric structure of the surface we choose a different perspective and view the surface from within the alloy. The square in the upper part of the surface is the remaining part of the initial condition which was covered by gold and therefore has not moved. Since the surface is shown from a direction inside the bulk, the portion of the bulk etched away is actually inside this surface. The time is chosen inversely proportional to $v_{\max}$, so that a uniform etching rate would have resulted in identical surfaces. Fig. 7 shows the cross sections for a higher velocity at various times. The picture in the middle shows the moment when the structure of the pit changes.

Example 3. This is a second numerical experiment on the small square of Example 2. While still focusing on the formation of a single pit, we want to start with a nonsymmetrical initial condition. So instead of using the previous initial condition, it is prepared by starting a simulation with a constant concentration of 10^{-7} on the surface and than evolving the system for 80 timesteps with a timestep size of 10^{-3}. During this evolution the same parameters as above are used, besides the value of $v_{\max} = 1.6$ and the concentration in the bulk, which is given by assigning random values between 0 and 24 to cubes of sidelength 0.05 below the initial surface. Starting with these parameters a single pit evolves which is neither circular nor contained in a plane (see right hand side of Fig. 5).

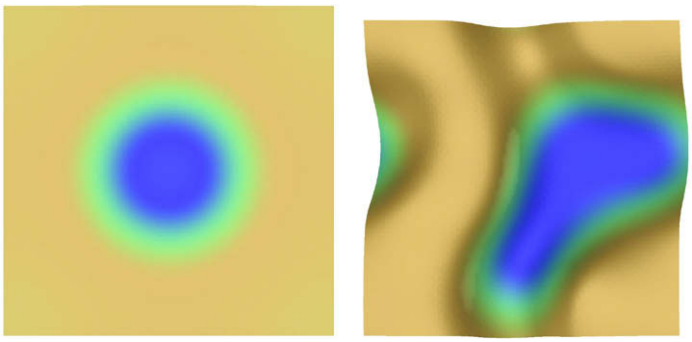

Fig. 5. Initial conditions for the second and for the last two experiments.

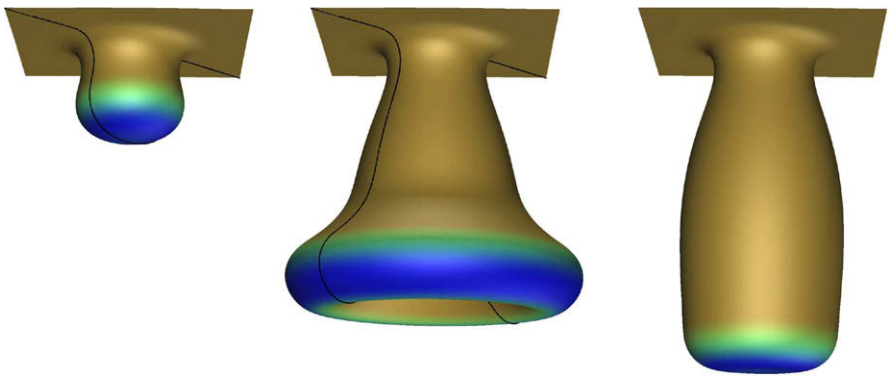

Fig. 6. Etching in a circular pit, $t = 0.25$ for $v_{\max} = 1.0$, $t = 0.75$ for $v_{\max} = 1.0$ and $t = 1.5$ for $v_{\max} = 0.5$.

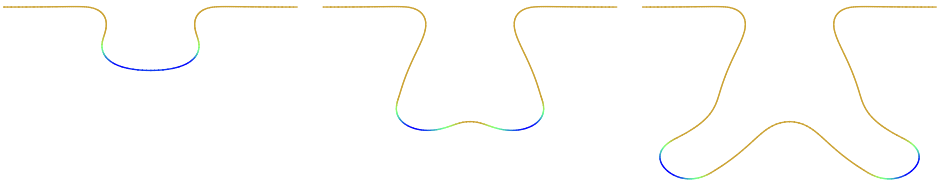

Fig. 7. Cross sections for example 2 and $v_{max} = 1.0,\ t = 0.25, t = 0.5$ and $t = 0.75$.

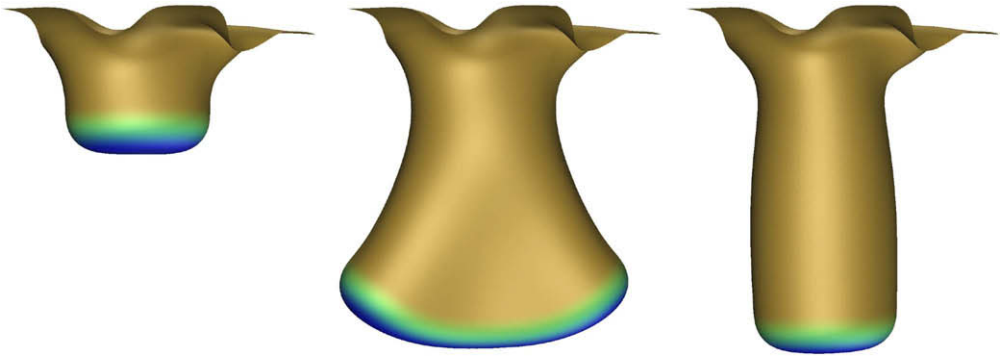

Fig. 8. Constant bulk concentration, $t = 0.25$ and $t = 0.75$ for $v_{max} = 1.0,\ t = 1.5$ for $v_{max} = 0.5$.

In the subsequent computation with this initial condition, the bulk concentration is taken to be constant, and v_{max} is varied during different simulations. Common to all chosen velocities is that there was no formation of a new component covered by gold in the the interior of the region etching into the bulk. For low velocities the evolution is similar to the one above, since the region actively etching into the bulk gets circular. For higher values of v_{max}, this region changed its shape by stretching into one direction. So this example shows another mechanism for increasing the complexity of the surface. Fig. 8 shows example for two different values of v_{max}. The perspective is similar to that of Fig. 6.

Example 4. In a third experiment on the small square, we study the effect of fluctuations of concentrations in the bulk on the evolution of the surface. So we start with the same initial condition as in the last experiment, but maintain a random concentration in the bulk during the whole simulation. At the beginning of the simulation the surface resembles the one of the last experiment. We still observe a velocity below which the shape of the gold poor region remains circular and returns to this shape after receiving small perturbations due to varying concentration in the bulk, see Fig. 9.

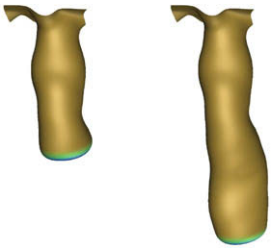

Fig. 9. Etching for a single pit, random bulk concentration, $t = 1.2$ and $t = 2.0$ for $v_{max} = 0.4$.

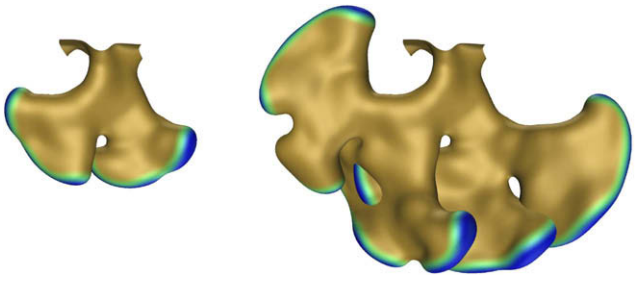

Fig. 10. Etching for a single pit, random bulk concentration, $t = 0.3$ and $t = 0.5$ for $v_{max} = 1.6$.

For larger values of v_{max}, the surface evolves to a much more complicated structure, Fig. 10. The number of components of the gold poor region on the surface increases, so the total area increases at a much higher rate, even when taking into account the higher value of v_{max}.

6. Conclusion

We have presented a novel numerical method for solving a nonlinear diffusion equation on a complex time dependent surface whose evolution is strongly coupled to the solution of the diffusion equation. The method is based on surface finite elements and triangulated surfaces. We implement methods to discretize the degenerate nonlinear Cahn-Hilliard equation and use adaptive grids within the computations. In order to have quasi-regular triangulations we present a method for retriangulating a periodic surface. Numerical simulations of the model for surface dissolution are presented which agree with the results of previous studies and indicate that the model can simulate the formation of complex morphology including porosity. It may be useful to consider numerical methods for solving partial differential equations on implicit surfaces, such as [8,9], in order to simulate the later stages where the interface morphology is much more complicated.

Acknowledgments

C. Eilks would like to thank Prof. G. Dziuk for an introduction to the topic and valuable discussions. This work was supported by the Deutsche Forschungsgemeinschaft via DFG-Forschungsgruppe *Nonlinear Partial Differential Equations: Theoretical and Numerical Analysis, Project A.1*. The numerical calculations were performed with the finite element toolbox `ALBERTA` [19], the graphical presentations were created with the package `geomview`.

References

[1] J.W. Barrett, J.F. Blowey, H. Garcke, Finite element approximation of the Cahn-Hilliard equation with degenerate mobility, SIAM J. Numer. Anal. 37 (1999) 286–318.
[2] M. Copetti, C.M. Elliott, Numerical analysis of the Cahn-Hilliard equation with a logarithmic free energy, Numer. Math. 63 (1992) 39–65.
[3] K.P. Deckelnick, G. Dziuk, C.M. Elliott, Computation of geometric PDEs and mean curvature flow, Acta Numer (2005) 139–232.
[4] J. Dogel, R. Tsekov, W. Freyland, Two dimensional connective nano-structures of electrodeposited Zn on Au (1 1 1) induced by spinodal decomposition, J. Chem. Phys. 122 (2005) 094703.
[5] G. Dziuk, Finite elements for the Beltrami operator on arbitrary surfaces, in: S. Hildebrandt, R. Leis (Eds.), (Herausgeber): Partial Differential Equations and Calculus of Variations. Lecture Notes in Mathematics, vol. 1357, Springer, Berlin, Heidelberg, New York, London, Paris, Tokyo, 1988, pp. 142–155.
[6] G. Dziuk, C.M. Elliott, Finite elements on evolving surfaces, IMA J. Numer. Anal. 27 (2007) 262–292.
[7] G. Dziuk, C.M. Elliott, Surface finite elements for parabolic equations, J. Comp. Math. 25 (2007) 385–407.
[8] G. Dziuk, C.M. Elliott, Eulerian finite element method for parabolic PDES on implicit surfaces, Interface. Free Bound. 10 (2008) 119–138.
[9] G. Dziuk, C.M. Elliott, Eulerian level set method for PDEs on evolving surfaces, Comput. Visual. Sci., in press, doi:10.1007/s00791-008-0122-0.
[10] G. Dziuk, An algorithm for evolutionary surfaces, Numer. Math. 58 (1991) 603–611.
[11] G. Dziuk, U. Clarenz, Numerical methods for conformally parametrized surfaces, Talk at CPDW04-Interphase 2003: numerical methods for free boundary problems. <www.newton.cam.ac.uk/webseminars/pg+ws/2003/CPDW04/0415/dziuk>.
[12] C.M. Elliott, D. French, F. Milner, A second order splitting method for the Cahn-Hilliard equation, Numer. Math. 54 (1989) 575–590.
[13] Xianfeng Gu, Shing-Tung Yau, Global conformal surface parameterization, in: SGP'03: Proceedings of the 2003 Eurographics/ACM SIGGRAPH Symposium on Geometry Processing, 2003, pp. 127–137.
[14] J. Erlebacher, An atomistic description of dealloying, J. Electrochem. Soc. 151 (10) (2004) C614–C626.
[15] J. Erlebacher, M.J. Aziz, A. Karma, N. Dimitrov, K. Sieradzki, Evolution of nanoporosity in dealloying, Nature 410 (2001) 450–453.
[16] J. Erlebacher, K. Sieradzki, Pattern formation during dealloying, Scripta Mater. 49 (2003) 991–996.
[17] P.L. Lions, B. Mercier, Splitting algorithms for the sum of two nonlinear operators, SIAM J. Numer. Anal. 16 (1979) 964–979.
[18] O. Schönborn, R.C. Desai, Kinetics of phase ordering on curved surfaces, Physica A 239 (1997) 412–419.
[19] A. Schmidt, K.G. Siebert, Design of Adaptive Finite Element Software: The Finite Element Toolbox ALBERTA, Lecture Notes in Computational Science and Engineering, vol. 42, Springer, 2004.
[20] Ping Tang, Feng Qiu, Hongdong Zhang, Yuliang Yang, Phase separation patterns for diblock copolymers on spherical surfaces: a finite volume method, Phys. Rev. E 72 (2005) 016710.